



Article

A Design Strategy for Surface Modification and Decarburization to Achieve Enhanced Mechanical Properties in Additively Manufactured Stainless Steel

Soumya Sridar ¹, Noah Sargent ¹, Stephanie Prochaska ², Mitra Shabani ¹, Owen Hildreth ^{3,*} and Wei Xiong ^{1,*}

- ¹ Physical Metallurgy and Materials Design Laboratory, Department of Mechanical Engineering and Materials Science, University of Pittsburgh, Pittsburgh, PA 15261, USA; sos57@pitt.edu (S.S.); nas188@pitt.edu (N.S.); mitra.shabani@pitt.edu (M.S.)
- ² Materials Science Program, Colorado School of Mines, 1500 Illinois St., Golden, CO 80401, USA; sprochaska@mines.edu
- ³ Department of Mechanical Engineering, Colorado School of Mines, Golden, CO 80401, USA
- * Correspondence: ohildreth@mines.edu (O.H.); weixiong@pitt.edu (W.X.); Tel.: +1-303-384-2457 (O.H.); +1-412-383-8092 (W.X.)

Abstract: Post-processing of additively manufactured components, including the removal of support structures and the reduction in surface roughness, presents significant challenges. Conventional milling struggles to access internal cavities, while the Self-Terminating Etching Process (STEP) offers a promising solution. STEP effectively smooths surfaces and dissolves supports without substantial changes in geometry. However, it can lead to compositional changes and precipitation, affecting the material properties and necessitating a design strategy to mitigate them. In this study, STEP is applied to stainless steel 316L (SS316L) produced via laser powder bed fusion, reducing surface roughness from 7 to 2 μm . After STEP, the surface carbon exhibited a threefold increase, leading to the formation of M_{23}C_6 clusters. This significantly impacted the yield strength, resulting in a 37% reduction compared to the as-built condition. The key to overcoming this challenge was using computational simulations, which guided the determination of the decarburization conditions: 1000 °C for 60 min, ensuring maximum M_{23}C_6 dissolution and surface carbon reduction with minimal grain coarsening. Following these conditions, the yield strength of SS316L was restored to the level observed in the as-built condition. These findings underscore the potential of the proposed design strategy to enhance the mechanical performance of additively manufactured components significantly.

Keywords: DICTRA; CALPHAD; dissolvable supports; surface roughness; laser powder bed fusion



Citation: Sridar, S.; Sargent, N.; Prochaska, S.; Shabani, M.; Hildreth, O.; Xiong, W. A Design Strategy for Surface Modification and Decarburization to Achieve Enhanced Mechanical Properties in Additively Manufactured Stainless Steel. *J. Manuf. Mater. Process.* **2024**, *8*, 264. <https://doi.org/10.3390/jmmp8060264>

Academic Editor: Steven Y. Liang

Received: 26 September 2024
Revised: 11 November 2024
Accepted: 18 November 2024
Published: 20 November 2024



Copyright: © 2024 by the authors. Licensee MDPI, Basel, Switzerland. This article is an open access article distributed under the terms and conditions of the Creative Commons Attribution (CC BY) license (<https://creativecommons.org/licenses/by/4.0/>).

1. Introduction

Support structures are essential in additive manufacturing (AM) for fabricating components with complex shapes. These structures anchor the part to the build plate during deposition, reducing distortion caused by thermal stresses and providing a thermal pathway for heat removal [1,2]. However, removing these necessary support structures can be difficult, expensive, and time-consuming. These additional operations can outweigh the benefits of AM, including reduced material wastage, high efficiency, and increased production flexibility [3,4]. This issue becomes a bottleneck for the manufacturing flexibility and sustainability enhancement of the AM technique. The laser powder bed fusion (LPBF) technique is a widely used AM process that involves successive layers of powder melted using a high-intensity laser beam [5]. For many parts built using LPBF, post-processing is necessary, including removing trapped powders and supports and reducing surface roughness.

Traditionally, post-processing methods such as mechanical grinding [6], laser treatments [7], and chemical etching-based approaches [8] are used to improve the surface finish of AM parts. Mechanical machining and abrasives are commonly used in mechanical-based

surface treatments involving deformation [9]. While deformation and laser-based techniques effectively reduce surface roughness, they cannot be used for complex geometries with inaccessible internal surfaces. Magnetic abrasive finishing was applied to successfully decrease the surface roughness of Inconel 718 fabricated using the laser powder bed fusion technique [10]. An improvement in the mechanical properties was observed after surface finishing. Yet, this method must be improved to apply to large parts since a long time will be required. Moreover, hybrid laser polishing was employed to improve the surface quality and surface microstructure of Inconel 718 fabricated by laser-directed energy deposition [11]. Chemical-based techniques can improve the surface finish of parts with internal surfaces. However, a non-uniform etching is expected since the etchant concentration decreases as the fluid moves from leading to trailing surfaces [12]. Therefore, dissolvable metal supports were developed for parts fabricated using AM. Initially, dissolvable metal supports were introduced using the multi-material directed energy deposition (DED) technique, where stainless steel arches were fabricated with low-carbon steel as the support material [13]. The lower chemical stability of low-carbon steel was utilized to selectively dissolve the support in an $\text{HNO}_3 + \text{KCl}$ solution, with an additional electrical bias to accelerate the dissolution process. This technique applies only to parts fabricated using AM techniques capable of multi-material deposition. A different approach called direct dissolution was developed for LPBF, typically limited to a single material. In this method, the support structures connected to a component over a small region (100–200 μm width) are electrochemically dissolved [14]. Yet, this approach can lead to significant pitting damage throughout the component and is not self-terminating. Additionally, critical process parameters such as etch rate, etch depth, and pitting can vary significantly with minor changes in component geometry, orientation, electrolyte viscosity, etc. [15,16].

To overcome the limitations of direct dissolution, the Self-Terminating Etching Process (STEP) was introduced to streamline the post-processing of LPBF components and maintain their geometry. The Hildreth group has formulated STEP protocols for various materials, including steel [17,18], nickel [19], titanium [20], and copper [21]. These protocols effectively remove large volumes of support structures, achieving surface roughness levels between 1 μm and 2 μm , while only eliminating a few micrometers from the surface. The process begins with printing the component using standard materials and LPBF parameters then exposure to a sensitizing agent and subsequent heat treatment. This leads to a compositional alteration in the outermost 20 to 150 μm of all surfaces, diminishing corrosion resistance and creating a “sensitized” layer selectively etched away, sparing the material beneath. For stainless steels, immersion in a saturated sodium hexacyanoferrate ($\text{Na}_4\text{Fe}(\text{CN})_6 \cdot 10\text{H}_2\text{O}$) solution is the sensitizing step. Heat treatment then causes the agent to decompose, forming a carbon layer that diffuses into the surface. This carbon captures chromium to form carbides within the top 50 to 150 μm , sensitizing the area by lowering the corrosion potential below that of stainless steel [22]. The sensitized region is then etched with an electrical bias, ensuring it dissolves anodically while the component below is cathodically protected. Ultimately, the supports and trapped powder are fully dissolved, and a thin, uniform layer is removed from the component—a factor accounted for in the pre-printing model. This technique applies to internal and external supports, reducing surface roughness and preserving the component shape.

While the method effectively removes support through selective dissolution, there is a possibility that the layer enriched with diffused carbon may not be entirely eliminated during etching. This necessitates measuring the surface carbon content post-etching and, if it exceeds the nominal level, designing an appropriate decarburization heat treatment. This study aims to quantify the carbon content on the surface of sensitized and etched SS316L, produced using the LPBF technique. The findings will inform the design of decarburization in Calculation of Phase Diagrams (CALPHAD)-type diffusion simulations, guiding subsequent experiments. Additionally, the proposed heat treatment is applied to the etched SS316L. The treatment efficacy is assessed by comparing the tensile properties before and after etching with those of as-printed and wrought SS316L. Surface roughness

is also measured to evaluate the impact of self-terminating etching on additively manufactured SS316L parts. The results indicate a promising approach to integrate surface modification with post-heat treatment, enhancing the mechanical performance of additively manufactured components.

2. Materials and Methods

2.1. Experimental Details

SS316L discs, 15 mm in diameter and 4 mm thick, were produced using an EOS M290 machine (EOS GmbH, Krailling, Germany) with the standard printing parameters: 100 W laser power, 675 mm/s scanning speed, 90 μm hatch spacing, and 40 μm layer thickness. The alloy powder composition (wt. %) provided by the vendor (Praxair Co., Danbury, CT, USA) includes C: 0.03, Cr: 17, Ni: 12, Mo: 2.5, Mn: 2, and Si: 1. Additionally, tensile bars conforming to ASTM E8 [23] (length: 100 mm, thickness: 6 mm, width: 10 mm, gauge length: 25 mm) standards were fabricated in a horizontal orientation for mechanical testing. These disc samples underwent the STEP process.

Two processing steps are included in STEP: sensitization and electrochemical etching, as shown in Figure 1. The samples were soaked for 20 min in a saturated solution of sodium hexacyanoferrate (II) decahydrate ($\text{Na}_4\text{Fe}(\text{CN})_6 \cdot 10\text{H}_2\text{O}$) and deionized (DI) water (18 M Ω , Thermo Scientific Smart2Pure 3 UV/UF) for sensitization. A thin layer of graphite powder was coated over 309 stainless steel tool wraps. The samples were packed in a slurry (4.2:1 mass ratio) of $\text{Na}_4\text{Fe}(\text{CN})_6 \cdot 10\text{H}_2\text{O}$ and DI water and wrapped into the wrap. $\text{Na}_4\text{Fe}(\text{CN})_6 \cdot 10\text{H}_2\text{O}$ produces CN and H_2O vapors on decomposition, and hence, small-sized holes were pierced to allow their release on the tool wrap. This package was placed inside the DT-22-FL-8-VA Deltech Front Loading Inert Gas Furnace and purged with argon gas three times. For dehydration of the sample, the furnace was heated at 5 K/min to 90, 185, and 250 $^\circ\text{C}$ with a holding time of 40, 60, and 60 min, respectively. Further, the furnace temperature was raised to 915 $^\circ\text{C}$ at 5 K/min and held for 6 h and 30 min for sensitization. The package containing the samples was quenched in water immediately after its removal from the furnace.

After sensitization, the samples were placed in a metal basket and held in close contact using wrapped SS316 wires. It is to be noted that this connection method is not as good as the epoxy-encapsulated method we have used for optimization studies [18]. However, it better mimics a more industrial process. The downside is those reaction products, such as chromium oxide, can build up between the component and the metal basket, which changes the potential that the part is held at, and, depending on contact resistance change, the resulting surface can be rougher than with an encapsulated contact. An electrolyte of 0.48 M nitric acid (HNO_3) and 0.1 M potassium chloride (KCl) in 1 L of DI water was prepared along with a 6.35 mm diameter graphite rod counter electrode. A KCl salt bridge was connected ionically with a silver/silver chloride (Ag/AgCl) reference electrode to the electrolyte. Electrochemical etching (chronoamperometry) was conducted using a Princeton Applied Research Parstat MC potentiostat with an applied potential of 550 mV_{SHE} (millivolt relative to standard hydrogen electrode) until the current density dropped to less than 1 mA/cm². The flowchart of the STEP technique is shown in Figure 1, along with the sensitization heat treatment schedule.

The surface roughness of the SS316L samples before and after etching was determined using a Keyence VR-3200 non-contact profilometer (Keyence Corporation, Itasca, IL, USA). The disc samples were cut along the build direction and stuck to aluminum mounts with hot glue rather than hot mounting to avoid carbon diffusion through the surface during mounting, affecting the subsequent carbon measurement. The cut sections were ground in 600, 800, and 1200 grit SiC emery papers, and the samples were polished further in diamond suspensions with particle sizes of 3 and 1 μm and a colloidal silica suspension of 0.04 μm particle size. The carbon content before and after the application of the designed decarburization heat treatment was measured using electron probe microanalysis (EPMA, JEOL JXA-8530F Field Emission Electron Probe Microanalyzer, JEOL, Peabody, MA, USA).

The measurement was performed for a length of $\sim 275 \mu\text{m}$ starting from the surface with an accelerating voltage of 7.3 kV, probe current of 50 nA, probe diameter of $3 \mu\text{m}$, and step size of $3 \mu\text{m}$. Steels with known carbon content were used for calibration [24]. In addition, a liquid nitrogen cold trap was used to prevent carbon contamination during the measurement. Microstructure characterization and determination of phase composition were carried out using a ZEISS Sigma 500 VP scanning electron microscope with an Oxford energy dispersive spectroscope (EDS) attached. X-ray diffraction (XRD) was performed on the surface of the samples using Bruker Discover D8 equipment with Cu K_{α} source in the 2θ range of 40 to 95° with a step size of 0.04° and a scan speed of 0.5 s/step . The grain structure was analyzed with electron backscattered diffraction (EBSD, EDAX Hickory EBSD system) connected to an FEI Scios Dual Beam focused ion beam–scanning electron microscope (SEM), with subsequent data analysis with TSL-OIM (version 8) software. Room temperature tensile tests were conducted using an MTS 880 universal testing machine with a 100 kN capacity for tensile bars (dimensions based on ASTM E8 standard [23]) and a strain rate of 10^{-3} s^{-1} . An extensometer for a 25 mm gauge length was employed for displacement measurement during the test.

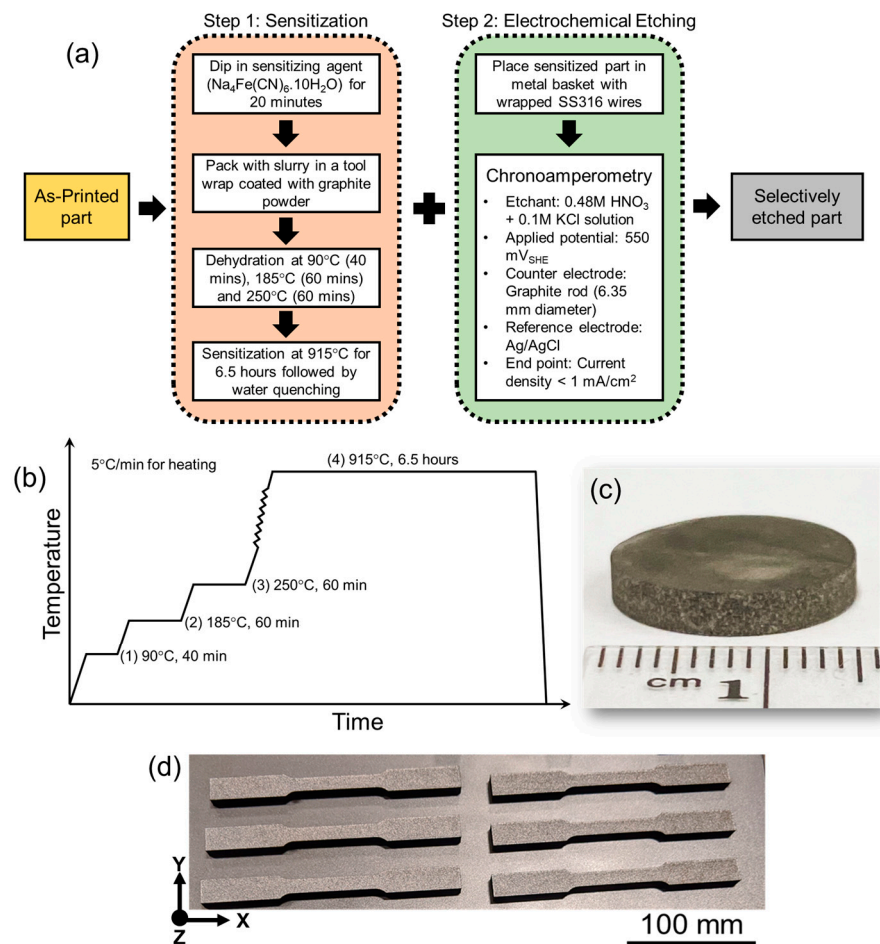


Figure 1. (a) Flowchart of the STEP technique applied to SS316L steel fabricated using the LPBF technique, (b) time–temperature profile used for sensitization heat treatment of SS316L steel (step 1 in (a)), (c) macrograph of the as-fabricated SS316L disc after application of the STEP technique, and (d) tensile bars of SS316L printed according to ASTM E8 standard in horizontal orientation using LPBF for the application of the STEP technique.

2.2. Computational Modeling

Diffusion simulation based on the diffusion module (DICTRA: Diffusion-Controlled Transformations) of the Thermo-Calc software (version 2021b) was used to guide the op-

timization of the parameters for decarburization heat treatment. The schematic of the simulation model setup is shown in Figure 2. The calculations were performed in the temperature range of 900 to 1100 °C in steps of 100 °C. As the matrix phase in the SS316L steel, the austenite (FCC) phase was considered for all temperatures. The thermodynamic and mobility databases used for these calculations were TCFE9 and MOBFE4, respectively. The simulations were performed for 5 h (18,000 s) with 100 grid points in accordance with the EPMA measurement. Additional inputs, such as the width of the cell, the position of grid points within the cell, and the carbon composition at each grid point, were chosen based on the results from the EPMA measurement. The composition of other alloying elements (Cr, Ni, Mo, Mn, and Si) in SS316L steel was measured using EDS in the same region where the EPMA measurements were performed and used as input for the kinetic simulations. To mimic the decarburizing atmosphere, the activity of carbon in the outer atmosphere interacting with the interface of the simulation cell was set to 10^{-6} .

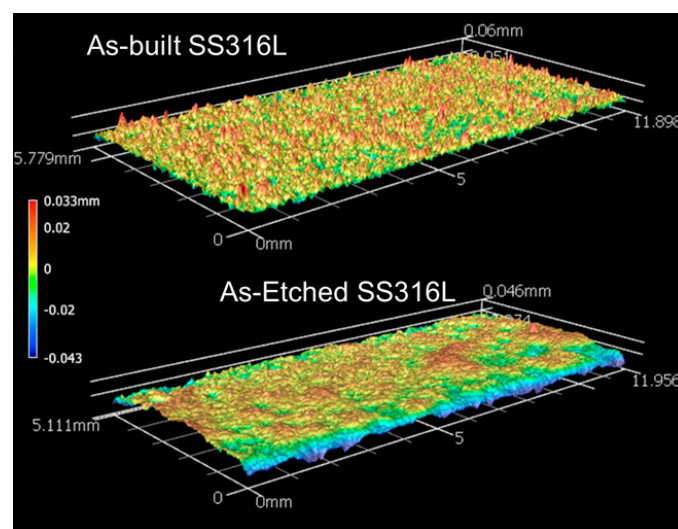


Figure 2. 3D-surface tomography maps for the as-built and as-etched SS316L show the difference in surface roughness, with sharp red peaks in the as-built condition and a relatively smoother surface without peaks in the as-etched condition.

3. Results

3.1. Characterization of As-Etched SS316L and Design of Decarburization

The 3D surface topography maps of SS316L, captured by the optical profilometer in as-built and as-etched conditions, are shown in Figure 2. The average roughness (R_a), representing the mean deviation between peaks and valleys, decreased from 7 μm in the as-built state to 2 μm post-etching. Similarly, R_z , the measure of the difference between the tallest peak and deepest valley, was reduced from 46 μm to 13 μm . These reductions confirm the efficacy of the STEP technique in diminishing the surface roughness of SS316L components produced by LPBF. The etching process has effectively leveled the surface, dissolving the peaks, as evidenced by the comparative surface topography maps in Figure 2. The as-built SS316L displays numerous sharp red peaks, which are substantially reduced in the as-etched sample.

Microstructural analysis of the as-etched SS316L steel surface was conducted using SEM on the cross-section of each sample, with micrographs captured in backscattered electron mode presented in Figure 3. Before the application of the STEP technique, the cross-section of the SS316L disc (Figure 3a) is clean without any secondary phases. On the other hand, numerous black features, rich in Cr as determined by EDS (Figure 4), can be observed near the surface along both vertical and horizontal edges (Figure 3b,c). These features appeared as a continuous network in certain areas and as isolated particles adjacent to the networks. The black features exhibited a higher Cr content (points 1–5) compared to

the Cr composition in the bulk sample (points 6–9), as detailed in the accompanying table (Figure 4). Consequently, it is inferred that these near-surface features are $M_{23}C_6$ (M: Cr, Fe) particles remaining post-STEP application to SS316L steel. These particles originated during the sensitization heat treatment shown in Figure 1b, which preceded etching to diminish the corrosion resistance of the surface.

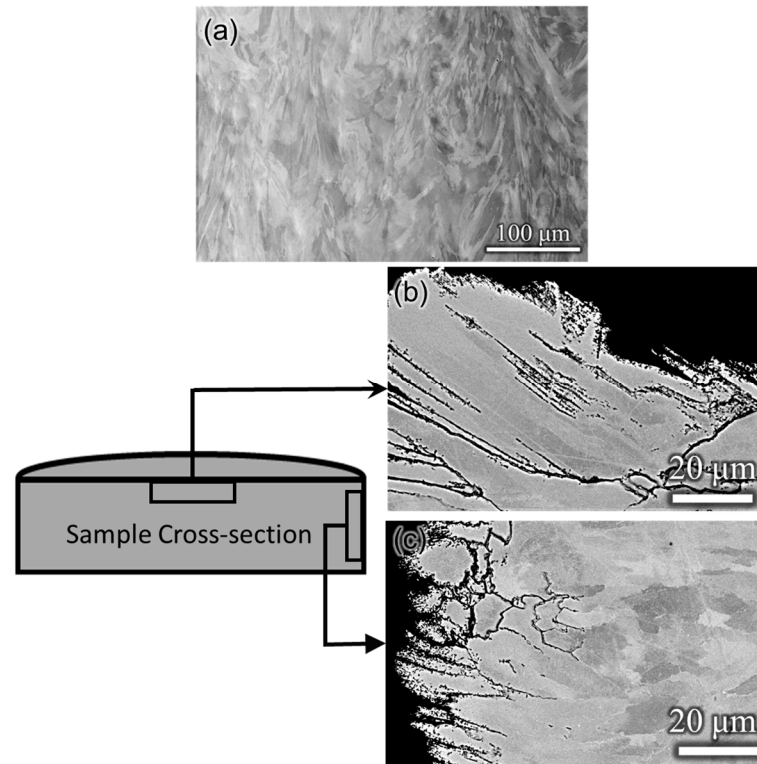


Figure 3. SEM micrograph of the (a) cross-section of the SS316L disc before application of STEP and those obtained from the (b) horizontal and (c) vertical edges of the as-etched SS316L steel show clusters of black features near the surface formed due to STEP.

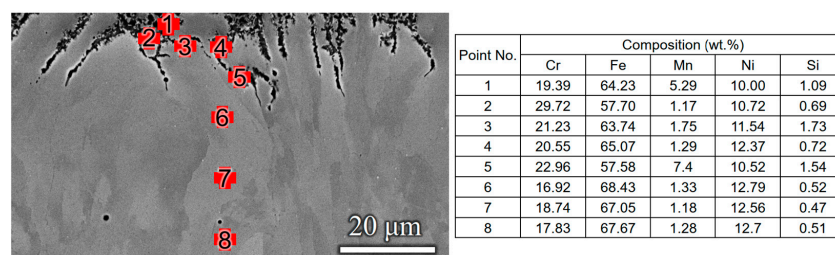


Figure 4. Composition measurements performed using EDS at different points from the surface to the bulk of the as-etched SS316L steel show that the black features correspond to the $M_{23}C_6$ phase with a higher chromium content than the bulk (refer to the table).

Carbon content on the etched sample surface was quantified using EPMA, as shown in Figure 5. EPMA measurements spanned three separate lines, each about 275 μm long, starting from the surface and moving into the sample bulk, as shown in the SEM image (Figure 5a). Along these lines, nearly 100 point measurements were performed, spaced 3 μm apart. Calculating the standard deviation of carbon content from multiple measurements provides a comprehensive understanding of compositional variations near the surface. Figure 5b displays the carbon composition gradient from the surface to the bulk, determined by EPMA, and includes the associated standard deviation. Notably, the surface carbon content is almost triple that of the bulk. These measurements underscore the importance

of a decarburization heat treatment post-etching to enhance SS316L properties produced via LPBF. Following the self-terminating etching of SS316L steel made with LPBF, the decarburization heat treatment fulfills two functions: it homogenizes the carbon content and dissolves $M_{23}C_6$ precipitates near the surface. This highlights the need for meticulous design of the decarburization to reduce the need for extensive experimental work to ascertain the optimal conditions for post-heat treatment.

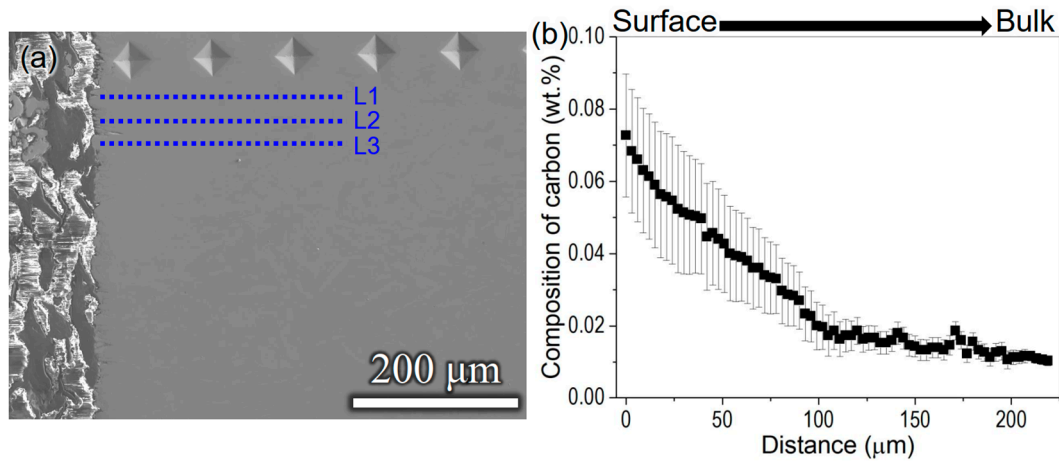


Figure 5. (a) SEM micrograph of as-etched SS316L steel showing the location of lines where the EPMA measurements were performed to determine the carbon content (hardness indents served as markers) and (b) variation in carbon content from the surface of the as-etched SS316L steel to the bulk showing three times increase in the composition of carbon close to the surface.

The decarburization treatment design was carried out using diffusion kinetic simulations with the Diffusion Controlled Transformations (DICTRA) module in the Thermo-Calc software (version 2021b). The main goal was to pinpoint the optimal time and temperature to reduce the accumulated surface carbon. Although the precise determination of heat treatment parameters is complex due to microstructural intricacies, DICTRA simulations offer essential guidance for preliminary experimental setups. It is crucial to acknowledge that these simulations cannot accurately model the dissolution of the $M_{23}C_6$ phase, as the necessary mobility parameters are not included in the commercially available multicomponent mobility databases. Figure 6 illustrates the predicted carbon content variation relative to distance based on different time and temperature scenarios from kinetic simulations. According to thermodynamic calculations, this figure also shows the calculated phase fractions at varying temperatures for SS316L powder. The required time to equalize the carbon content from the surface to the bulk was found to be 600, 120, and 60 s at temperatures of 900, 1000, and 1100 °C, respectively, as shown in Figure 6a–c. Additionally, the dissolution temperature for $M_{23}C_6$ was identified at 960 °C (Figure 6d). Consequently, a practical temperature for the decarburization heat treatment was set at 1000 °C, which exceeds the $M_{23}C_6$ dissolution temperature and prevents excessive grain growth. At this temperature, the carbon level reduction to the desired amount was calculated to take 120 s. Nonetheless, a longer duration may be required to dissolve $M_{23}C_6$ particles completely. Hence, while kinetic and thermodynamic simulations have ascertained the ideal decarburization temperature, experimental validation is imperative to determine the precise duration needed, especially considering the complexities of $M_{23}C_6$ dissolution.

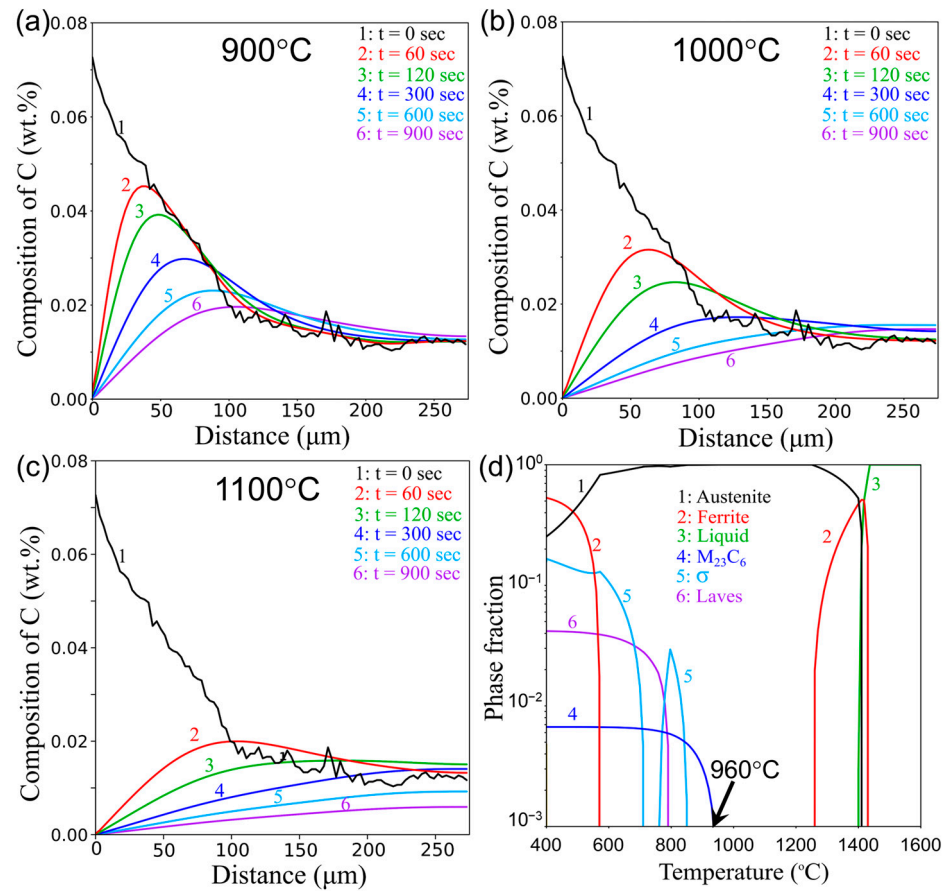


Figure 6. Carbon content as a function of distance for different times determined using kinetic simulations at (a) 900, (b) 1000, and (c) 1100 °C showing the optimum decarburization times as well as (d) calculated phase fraction as a function of temperature for SS316L steel powder showing the dissolution temperature of M₂₃C₆ phase.

3.2. Application of Designed Decarburization and Property Evaluation

Having established the optimal decarburization temperature as 1000 °C through prior computational analysis, it is now essential to refine our understanding of the ideal decarburization time through systematic experimental investigations. Moreover, determining the suitable atmosphere for the decarburization process is crucial. Consequently, decarburization was carried out at 1000 °C under two distinct atmospheres: flowing air and vacuum, each for varying durations (30, 60, and 120 min). Flowing air was selected due to its well-documented efficacy in reducing carbon content in steels. This is achieved through the formation and subsequent release of CO gas generated by the reaction between the excess surface carbon and atmospheric oxygen. The composition maps, obtained through EDS analysis, for the SS316L sample subjected to decarburization at 1000 °C for 30 min in flowing air, as shown in Figure 7a, clearly indicate the presence of a substantial layer of Cr-rich oxide, whereas in the vacuum atmosphere, no significant oxidation was observed (Figure 7b). Given that the sample subjected to the shortest decarburization duration already exhibited oxidation, it is reasonable to assume that samples exposed to longer decarburization times (60 and 120 min) would also experience comparable or even worse surface oxidation. This observation highlights the inadequacy of decarburizing SS316L steel in a flowing air environment, primarily attributed to the formation of a substantial Cr-rich oxide layer on the steel surface.

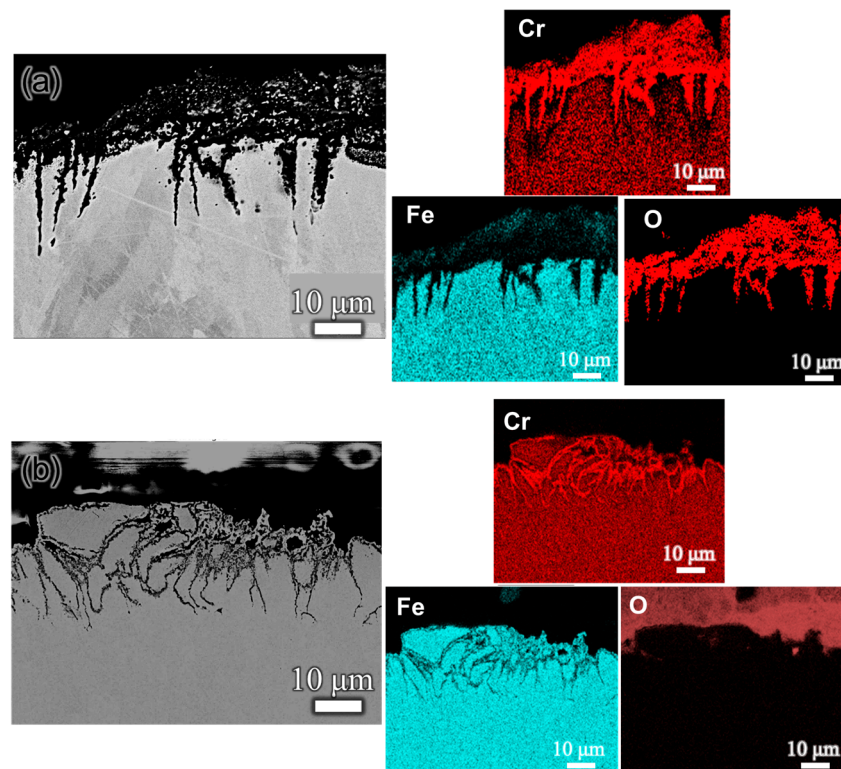


Figure 7. Composition maps obtained using EDS from the surface of SS316L decarburized after etching at 1000 °C for 30 min in (a) flowing air showing the formation of a Cr-rich oxide layer and (b) in a vacuum atmosphere without any significant oxidation.

Conversely, SS316L samples decarburized at 1000 °C for various durations (30, 60, and 120 min) in a vacuum atmosphere exhibited no oxide layer formation on the surface. Additionally, EPMA was employed to measure the surface carbon content post-decarburization. Measurements were taken along three distinct lines, mirroring the approach used for the as-etched sample, to ascertain the standard deviation in carbon content. As shown in Figure 8, the carbon content gradient from the surface to the bulk of the decarburized samples is presented alongside the surface carbon content of the as-etched sample for comparison. The data clearly indicate that the surface carbon content aligns with the bulk composition for all SS316L samples decarburized at 1000 °C in a vacuum, regardless of the duration. This confirms the efficacy of the decarburization temperature determined through computational analysis. While each tested duration successfully reduced the surface carbon content of SS316L steel, additional microstructural analysis is necessary to identify the optimal decarburization time. In addition, it is evident from the XRD analysis that the matrix phase is FCC, with the peaks observed corresponding to that phase.

Inverse pole figure (IPF) maps, generated using EBSD to reveal the grain structure of SS316L samples decarburized at 1000 °C in a vacuum for varying durations, are displayed in Figure 9. These maps show that post-decarburization grains are more rounded compared to the columnar grains typically formed during the LPBF process in SS316L steel, as seen in Figure 9a–d. The aspect ratios (length/width) of a minimum of 20 grains measured using the ImageJ software (version 15.3) for the as-built sample and the sample decarburized for 30 min were found to be 5.88 ± 1.07 and 1.80 ± 0.58 , respectively, proving the roundness of the grains. This change is attributed to the sensitization treatment conducted at 915 °C. Average grain sizes for the various decarburization conditions were calculated from IPF maps across three distinct regions using the TSL-OIM software (version 7). The grain size plot indicates significant coarsening in the sample decarburized for 120 min, with an approximate 10% increase in grain size relative to the 60 min sample. Conversely, the sample decarburized for 60 min exhibits a modest increase in grain size (~2%) compared

to the 30 min sample. Therefore, a decarburization duration of 120 min at 1000 °C in a vacuum is not optimal due to the pronounced grain coarsening.

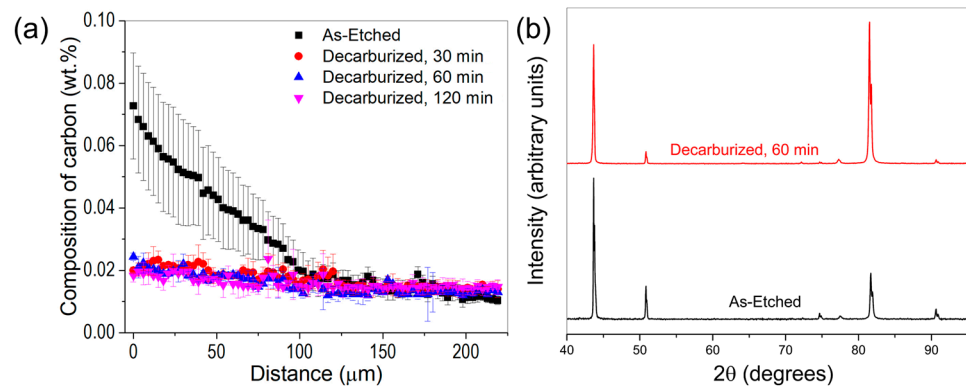


Figure 8. (a) Variation in carbon content along with standard deviation for the as-etched sample and the samples decarburized in a vacuum at 1000 °C for different times showed that the accumulated carbon in the surface evened out for all the time periods tested in this work and (b) XRD analysis of the as-etched sample and sample decarburized for 60 min at 1000 °C showing an FCC matrix phase.

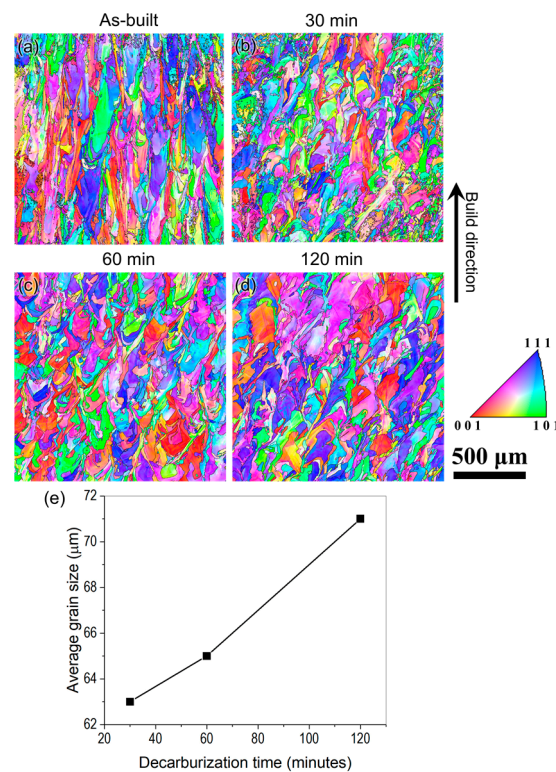


Figure 9. IPF maps for SS316L samples in (a) as-built condition and decarburized at 1000 °C in a vacuum for (b) 30, (c) 60, and (d) 120 min as well as (e) plot for variation in grain size as a function of decarburization time obtained using EBSD measurements showing that the grains in decarburized samples are more rounded than the as-built sample and excessive grain coarsening occurs after decarburization for 120 min.

Subsequent microstructural analysis near the surface of SS316L steel decarburized for 30 and 60 min was performed to determine the optimal decarburization time between these two conditions, as illustrated in Figure 10. The SEM micrograph near the surface of the 30 min decarburized sample reveals black features akin to those in the as-etched sample (Figure 4), corresponding to $M_{23}C_6$ carbides, as shown in Figure 10a. Although the

surface carbon content has decreased, a considerable number of $M_{23}C_6$ particles remain near the surface after decarburization at 1000 °C for 30 min in a vacuum. In contrast, the microstructure near the surface of the 60 min decarburized sample shows no such features, as depicted in Figure 10b. Additionally, a high-magnification image (Figure 10c) indicates the presence of a few small, discontinuous $M_{23}C_6$ particles at grain boundaries and within grains, which is unlikely to impact the properties significantly. Therefore, based on grain structure analysis after microstructural characterization near the surface, the optimal decarburization time at 1000 °C in a vacuum is established at 60 min.

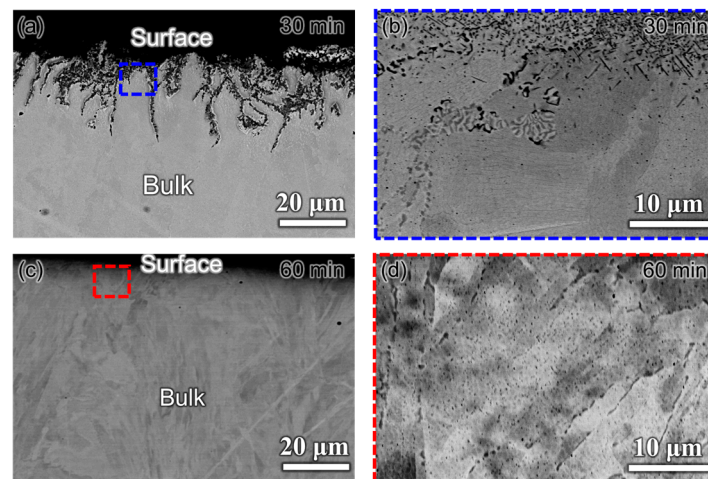


Figure 10. SEM micrographs from the surface of the sample decarburized in a vacuum at 1000 °C for (a) 30 min, (b) high magnification micrograph of the region close to the surface of the sample decarburized for 30 min showing large amounts of undissolved $M_{23}C_6$ particles, (c) surface of the sample decarburized in a vacuum at 1000 °C for 60 min showing that there is an effective dissolution of the $M_{23}C_6$ particles forming large clusters, and (d) high-magnification micrograph of the region close to the surface of the sample decarburized for 60 min showing the presence of a minor amount of discontinuous $M_{23}C_6$ in grain boundaries and within the grains.

To evaluate the effectiveness of the designed decarburization heat treatment to be applied after self-terminating etching in this work, the mechanical properties of SS316L in different conditions were determined. The engineering stress–strain curves and the tensile properties of as-built, as-etched, etched + decarburized, and wrought conditions are shown in Figure 11. It is to be noted that all the tensile bars were homogenized at 1200 °C for 1 h before application of the self-terminating etching process for the following reason. The as-built microstructure is highly columnar for additively manufactured SS316L (Figure 9a), allowing the carbon to penetrate deep into the alloy and increase the intergranular corrosion rate. This results in higher material loss and a rougher surface with sharp crack initiation sites. After applying the homogenization treatment, the grains become more rounded (Figure 9). Hence, any intergranular corrosion follows a rounded path that reduces the roughness and number of crack initiation sites. The homogenization temperature and time were chosen based on the report by Fonda et al. [25], where they have proved that homogenization of additively manufactured SS316L at 1200 °C for 1 h leads to recrystallization of the columnar grain structure and the least grain coarsening.

From the tensile properties summarized in Figure 11, it can be observed that the yield strength drops drastically by ~30% in comparison with the as-built sample with the application of STEP treatment to SS316L steel. However, the ultimate tensile strength and ductility remained unaffected. This behavior can be attributed to the formation of surface cracks in the as-etched samples due to the presence of a high density of $M_{23}C_6$ carbides on the surface, as shown in Figure 4, which will reduce the yield strength. With the application of the designed decarburization heat treatment after STEP, it can be found that the yield strength improved such that it is close to its corresponding value in the

as-built condition, and the ultimate tensile strength increased substantially. The static toughness, determined by calculating the area under the stress–strain curve in the plastic region, was also the highest in the etched + decarburized condition. The yield strength and ultimate tensile strength of the as-etched and etched + decarburized conditions were much higher than the corresponding values of wrought SS316L, proving that STEP treatment does not downgrade the tensile properties excessively. From the fracture surfaces observed using SEM (Figure 12), it can be observed that ductile fractures with dimples of varying sizes are typical of SS316L for all conditions. Therefore, the designed decarburization heat treatment successfully improved the properties of additively manufactured SS316L after surface treatment, such as STEP. This also necessitates developing an appropriate post-heat treatment process to recover the properties that are downgraded due to surface treatment.

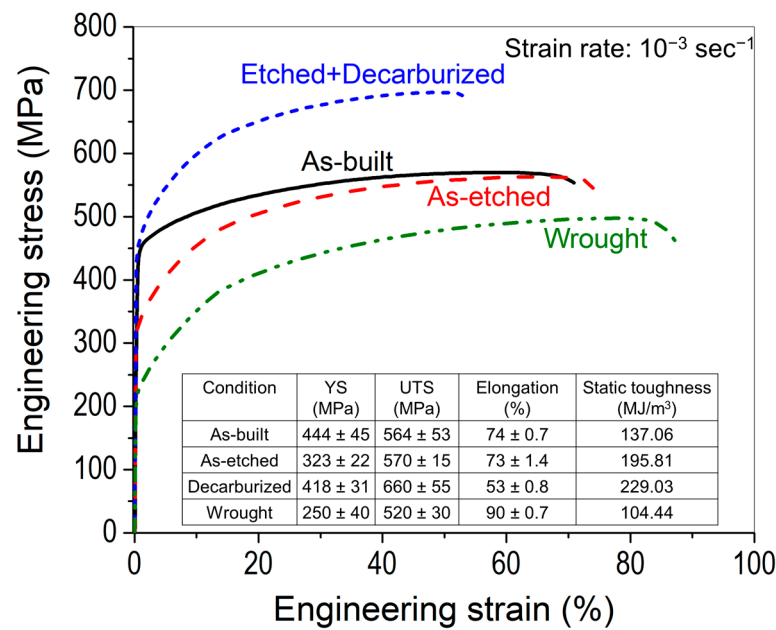


Figure 11. Engineering stress–strain curves and the tensile properties of as-built, as-etched, etched + decarburized, and wrought SS316L steel show that the designed decarburization heat treatment has helped in restoring the strength that was reduced due to the application of the etching treatment.

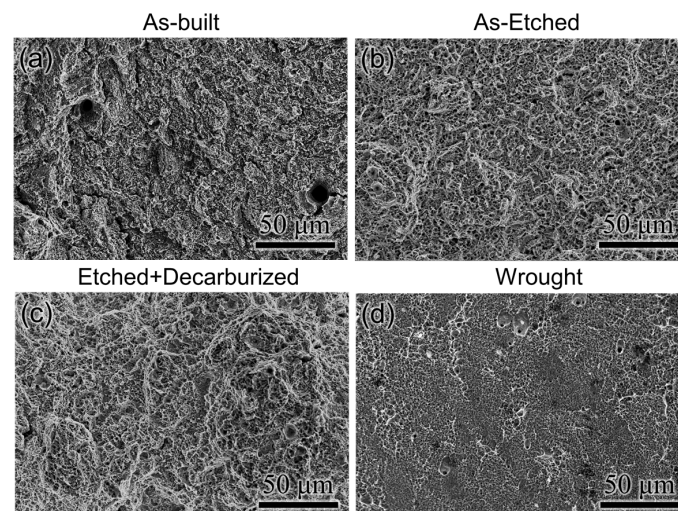


Figure 12. SEM micrographs of the fracture surface in (a) as-built, (b) as-etched, (c) etched + decarburized, and (d) wrought conditions after tensile tests showing ductile fracture with dimples in all conditions.

4. Conclusions

This study applied STEP to SS316L steel produced via the LPBF process, successfully reducing surface roughness from 7 μm in the as-built state to 2 μm post-etching. Additionally, residual M_{23}C_6 carbide particles were detected at the edges, and the surface carbon content was found to be threefold that of the bulk after STEP. Kinetic simulations, utilizing CALPHAD-based DICTRA with input from the as-etched carbon, were conducted to design a decarburization strategy to eliminate the excess carbon and dissolve the M_{23}C_6 particles near the surface. The optimal decarburization temperature was established at 1000 °C through DICTRA simulations in the Thermo-Calc software (version 2021b). Experimental decarburization at 1000 °C revealed that flowing air led to the formation of a Cr-rich oxide layer, rendering it ineffective. In contrast, vacuum decarburization aligned the surface carbon content with the bulk across all tested durations; however, grain coarsening was significant after 120 min, and M_{23}C_6 particles did not dissolve after 30 min. Thus, the ideal decarburization time was determined to be 60 min at 1000 °C in a vacuum. Although the yield strength decreased markedly following STEP compared to the as-built SS316L steel, the subsequent tailored decarburization restored the tensile properties to levels comparable to the as-built condition. This emphasizes the critical importance of a well-designed post-heat treatment following surface modification to enhance the mechanical properties of additively manufactured alloys.

Author Contributions: Conceptualization, W.X. and O.H.; methodology, W.X. and O.H.; software, S.S.; validation, S.S., N.S., S.P. and M.S.; formal analysis, S.S., N.S., S.P. and M.S.; investigation, S.S., N.S., S.P. and M.S.; resources, W.X. and O.H.; data curation, S.S., N.S., S.P. and M.S.; writing—original draft preparation, S.S.; writing—review and editing, S.S., N.S., S.P., M.S., O.H. and W.X.; visualization, S.S. and N.S.; supervision, W.X. and O.H.; project administration, W.X. and O.H.; funding acquisition, W.X. and O.H. All authors have read and agreed to the published version of the manuscript.

Funding: This research was funded by the Nuclear Energy University Program (NEUP), Department of Energy—Office of Nuclear Energy, United States, grant number DE-NE0008813 and the National Science Foundation, United States, grant number 1944516.

Data Availability Statement: The original contributions presented in the study are included in the article; further inquiries can be directed to the corresponding authors.

Conflicts of Interest: The authors declare no conflicts of interest.

References

- Griffith, M.L.; Harwell, L.D.; Romero, J.T.; Schlienger, E.; Atwood, C.L.; Smugeresky, J.E. Multi-Material Processing By LENS. In Proceedings of the International Solid Freeform Fabrication Symposium, Austin, TX, USA, 11–13 August 1997; pp. 387–394.
- Wang, D.; Yang, Y.; Yi, Z.; Su, X. Research on the Fabricating Quality Optimization of the Overhanging Surface in SLM Process. *Int. J. Adv. Manuf. Technol.* **2012**, *65*, 1471–1484. [[CrossRef](#)]
- Gu, D.D.; Meiners, W.; Wissenbach, K.; Poprawe, R. Laser Additive Manufacturing of Metallic Components: Materials, Processes and Mechanisms. *Int. Mater. Rev.* **2012**, *57*, 133–164. [[CrossRef](#)]
- Herzog, D.; Seyda, V.; Wycisk, E.; Emmelmann, C. Additive Manufacturing of Metals. *Acta Mater.* **2016**, *117*, 371–392. [[CrossRef](#)]
- Gorsse, S.; Hutchinson, C.; Gouné, M.; Banerjee, R. Additive Manufacturing of Metals: A Brief Review of the Characteristic Microstructures and Properties of Steels, Ti-6Al-4V and High-Entropy Alloys. *Sci. Technol. Adv. Mater.* **2017**, *18*, 584–610. [[CrossRef](#)]
- Khan, H.M.; Karabulut, Y.; Kitay, O.; Kaynak, Y.; Jawahir, I.S. Influence of the Post-Processing Operations on Surface Integrity of Metal Components Produced by Laser Powder Bed Fusion Additive Manufacturing: A Review. *Mach. Sci. Technol.* **2021**, *25*, 118–176. [[CrossRef](#)]
- Gisario, A.; Barletta, M.; Veniali, F. Laser Polishing: A Review of a Constantly Growing Technology in the Surface Finishing of Components Made by Additive Manufacturing. *Int. J. Adv. Manuf. Technol.* **2022**, *120*, 1433–1472. [[CrossRef](#)]
- Jamshidi, P.; Aristizabal, M.; Kong, W.; Villapun, V.; Cox, S.C.; Grover, L.M.; Attallah, M.M. Selective Laser Melting of Ti-6Al-4V: The Impact of Post-Processing on the Tensile, Fatigue and Biological Properties for Medical Implant Applications. *Materials* **2020**, *13*, 2813. [[CrossRef](#)]
- Maleki, E.; Bagherifard, S.; Bandini, M.; Guagliano, M. Surface Post-Treatments for Metal Additive Manufacturing: Progress, Challenges, and Opportunities. *Addit. Manuf.* **2021**, *37*, 101619. [[CrossRef](#)]

10. Zhao, Y.; Ratay, J.; Li, K.; Yamaguchi, H.; Xiong, W. Effects of Magnetic Abrasive Finishing on Microstructure and Mechanical Properties of Inconel 718 Processed by Laser Powder Bed Fusion. *J. Manuf. Mater. Process.* **2022**, *6*, 43. [[CrossRef](#)]
11. Liu, Y.; Ouyang, W.; Wu, H.; Xu, Z.; Sheng, L.; Zou, Q.; Zhang, M.; Zhang, W.; Jiao, J. Improving Surface Quality and Superficial Microstructure of LDED Inconel 718 Superalloy Processed by Hybrid Laser Polishing. *J. Mater. Process. Technol.* **2022**, *300*, 117428. [[CrossRef](#)]
12. Raikar, S.; Digregorio, S.; Agnani, M.; Hommer, G.M.; Hildreth, J. Improving Fatigue Performance of Additively Manufactured Ti-6Al-4V Using Sulfur-Based Self-Terminating Etching Processes. *Addit. Manuf.* **2023**, *61*, 103331. [[CrossRef](#)]
13. Hildreth, O.J.; Nassar, A.R.; Chasse, K.R.; Simpson, T.W. Dissolvable Metal Supports for 3D Direct Metal Printing. *3D Print. Addit. Manuf.* **2016**, *3*, 91–97. [[CrossRef](#)]
14. Lefky, C.S.; Nassar, A.R.; Simpson, T.; Hildreth, O.J. Dissolvable Metal Supports for Printed Metal Parts. In Proceedings of the Solid Freeform Fabrication 2016: The 27th Annual International Solid Freeform Fabrication Symposium—An Additive Manufacturing Conference, SFF 2016, Austin, TX, USA, 8–10 August 2016; pp. 1604–1610.
15. Vanýsek, P. Impact of Electrode Geometry, Depth of Immersion, and Size on Impedance Measurements. *Can. J. Chem.* **2011**, *75*, 1635–1642. [[CrossRef](#)]
16. Zhang, F.; Liu, J.; Ivanov, I.; Hatzell, M.C.; Yang, W.; Ahn, Y.; Logan, B.E. Reference and Counter Electrode Positions Affect Electrochemical Characterization of Bioanodes in Different Bioelectrochemical Systems. *Biotechnol. Bioeng.* **2014**, *111*, 1931–1939. [[CrossRef](#)]
17. Hoffman, R.; Hinnebusch, S.; Raikar, S.; To, A.C.; Hildreth, O.J. Support Thickness, Pitch, and Applied Bias Effects on the Carbide Formation, Surface Roughness, and Material Removal of Additively Manufactured 316 L Stainless Steel. *JOM* **2020**, *72*, 4254–4263. [[CrossRef](#)]
18. Prochaska, S.; Hildreth, O. Effect of Chemically Accelerated Vibratory Finishing on the Corrosion Behavior of Laser Powder Bed Fusion 316L Stainless Steel. *J. Mater. Process. Technol.* **2022**, *305*, 117596. [[CrossRef](#)]
19. Lefky, C.S.; Gallmeyer, T.G.; Moorthy, S.; Stebner, A.; Hildreth, O.J. Microstructure and Corrosion Properties of Sensitized Laser Powder Bed Fusion Printed Inconel 718 to Dissolve Support Structures in a Self-Terminating Manner. *Addit. Manuf.* **2019**, *27*, 526–532. [[CrossRef](#)]
20. Raikar, S.; Heilig, M.; Mamidanna, A.; Hildreth, O.J. Self-Terminating Etching Process for Automated Support Removal and Surface Finishing of Additively Manufactured Ti-6Al-4 V. *Addit. Manuf.* **2021**, *37*, 101694. [[CrossRef](#)]
21. Thomas, S.; Hildreth, O.; Asle Zaeem, M. Unveiling the Effect of Vacancy Defects on Structural, Mechanical, Electronic and Diffusion Properties of Copper (I) Iodide. *Scr. Mater.* **2022**, *213*, 94–99. [[CrossRef](#)]
22. Parvathavarthini, N.; Mudali, U.K. Electrochemical Techniques for Estimating the Degree of Sensitization in Austenitic Stainless Steels. *Corros. Rev.* **2014**, *32*, 183–225. [[CrossRef](#)]
23. *ASTM E8/E8M22*; Standard Test Methods for Tension Testing of Metallic Materials—Designation. American Society for Testing and Materials: West Conshohocken, PA, USA, 2004.
24. Yamashita, T.; Tanaka, Y.; Yagoshi, M.; Ishida, K. Novel Technique to Suppress Hydrocarbon Contamination for High Accuracy Determination of Carbon Content in Steel by FE-EPMA. *Sci. Rep.* **2016**, *6*, 29825. [[CrossRef](#)]
25. Fonda, R.W.; Rowenhorst, D.J.; Feng, C.R.; Levinson, A.J.; Knipling, K.E.; Olig, S.; Ntiros, A.; Stiles, B.; Rayne, R. The Effects of Post-Processing in Additively Manufactured 316L Stainless Steels. *Metall. Mater. Trans. A Phys. Metall. Mater. Sci.* **2020**, *51*, 6560–6573. [[CrossRef](#)]

Disclaimer/Publisher’s Note: The statements, opinions and data contained in all publications are solely those of the individual author(s) and contributor(s) and not of MDPI and/or the editor(s). MDPI and/or the editor(s) disclaim responsibility for any injury to people or property resulting from any ideas, methods, instructions or products referred to in the content.